BUTTERWORTH
HEINEMANN

Large-eddy simulation of turbulent heat transport in enclosed impinging jets

Shian Gao
Department of Engineering, University of Leicester, Leicester, UK

Peter R. Voke
Department of Mechanical Engineering, The University of Surrey, Guildford, UK

The results of large-eddy simulation (LES) of thermally inhomogeneous jets issuing into an enclosed pool and impinging on a plate are presented. The LES has been performed by strongly conservative linear finite-volume techniques, with a simple subgrid-scale model. Several cases have been simulated with different geometries of the outflows at either side of the plate, or with different fluid properties. The mechanisms by which thermal eddies are formed and transported into the impingement zone have been fully elucidated for one of the simulated cases through graphic and video output of the thermal field. The reason for the very high lateral correlations found in the experiments and confirmed by LES results is explained convincingly in terms of the altered shape of thermal eddies as they convect toward the plate.

Keywords: large-eddy simulation; impinging jets; heat transfer; thermal structures

Introduction

Large-eddy simulation (LES) is increasingly recognized as a major tool for studying details of turbulent engineering flows. This method integrates the three-dimensional (3-D) time-dependent Navier–Stokes equations directly to resolve the large (grid-scale) eddies, while the small (subgrid-scale) eddies that cannot be resolved on the grid are represented by a subgrid model. Therefore, LES can be applied to complex engineering flows at high Reynolds numbers. Direct numerical simulation (DNS), which does not rely on any empirical model, is able to solve all the physical scales of flows, but is restricted to flows of very low Reynolds numbers owing to the limited computational resources available. Since both direct and large-eddy simulations contain time-dependent information such as evolution of large eddies in three dimensions, instantaneous fluctuations, time traces of quantities, spectra, and two-point correlations, they can give a much more realistic picture of certain aspects of the turbulence than traditional methods of turbulence prediction, which yield only averaged values, such as mean velocity and mean temperature fluctuations.

The impingement of heated turbulent fluid on solid structures occurs in a number of industrial contexts including power engineering, chemical engineering, and aeronautical engineering. The interaction of heated fluid and supporting structures can result in the thermal fluctuations in the fluid being transmitted to the solid, producing varying thermal stresses that are difficult to predict. This effect, known as thermal striping, is of considerable importance to the operation and safety of fast reactors, where the liquid sodium emerging from the reactor core is much hotter and faster than the sodium from the breeding blanket. The turbulent mixing fluid impinges on the above-core structure, which could result in thermal fatigue and eventually failure of the structure.

It is believed that thermal striping effects are governed by occasional large temperature swings. Such information is beyond the reach of such prediction methods as closure modeling. In our studies, the normal impingement of a thermally inhomogeneous plane jet, either of water impinging on perspex or of liquid sodium on steel, has been computed by LES. The Reynolds number of the simulation is about 6,500, based on the jet half-width and mean velocity at jet efflux plane. The flows simulated match a set of jet-in-pool experiments by Morss (1991), although the geometry is planar instead of cylindrical. To assess the effects of the geometrical difference between the experiment and simulation, closure modeling has been carried out by Ushijima (1991) in both cylindrical and planar geometries using an independent code with a two-equation model.

The main objective of the project was to elucidate the mechanisms by which thermal eddies are generated and transported into the impingement region in order to understand the thermal interaction between the fluid and solid. The effects of Prandtl number on the dynamics of the heat transfer are reported elsewhere (Gao et al. 1991).

Numerical methods

Finite-volume code

The finite-volume code used for this study is capable of simulating 3-D time-dependent turbulent flows having a single statistically homogeneous dimension. The other two dimensions can involve spatial development, solid walls, or strong shear. The code conserves momentum and advected kinetic energy to high accuracy, while computing the momentum fluxes across cell boundaries and the volume mean pressures approximately to second order in the mesh size.

Address reprint requests to Dr. P. R. Voke, Department of Mechanical Engineering, The University of Surrey, Guildford, Surrey GU2 5XH, UK.

Received 30 January 1995; accepted 12 May 1995

Int. J. Heat and Fluid Flow 16: 349–356, 1995

655 Avenue of the Americas, New York, NY 10010

0142-727X/95/$10.00
SSDI 0142-727X(95)00050-Z

The incompressible Navier–Stokes equations are discretised on a staggered mesh (Schumann 1975) with central interpolation in space, and integrated explicitly in time to second order using the Adams–Bashforth algorithm:

$$u_i^* = u_i^n + \Delta t\left(\frac{3}{2}H_i^n - \frac{1}{2}H_i^{n-1}\right) \tag{1}$$

$$u_i^{n+1} = u_i^* - \Delta t\frac{\Delta p^*}{\Delta x} \tag{2}$$

where

$$H_i = \frac{\Delta}{\Delta x_j}\left[-u_i u_j + 2(\nu_m + \nu_s)s_{ij}\right] \tag{3}$$

$$s_{ij} = \frac{1}{2}\left(\frac{\Delta u_i}{\Delta x_j} + \frac{\Delta u_j}{\Delta x_i}\right) \tag{4}$$

Superscripts n indicate the time step. ν_m is the molecular viscosity and ν_s is the subgrid-scale eddy viscosity. u_i^* is an intermediate velocity field which does not generally obey continuity. We take account of this through the pressure calculation. Taking the divergence of Equation 2 and noting that the new velocity field u_i^{n+1} must possess a zero divergence in every computation cell, we obtain a discrete Poisson equation for the pressure field:

$$\partial^2 p^* = \frac{1}{\Delta t}\frac{\Delta u_i^*}{\Delta x_i} \tag{5}$$

The above equation is Fourier transformed in the z direction, and then solved by a vectorized cyclic reduction method in the x and y directions following the algorithms of Schwarztrauber (1974), which allow for nonuniform meshes in these directions. The thermal field is computed as a passive contaminant, the discretization being similar to that for the momentum equations

$$T^{n+1} = T^n + \Delta t\left(\frac{3}{2}H_T^n - \frac{1}{2}H_T^{n-1}\right) \tag{6}$$

where

$$H_T = \frac{\Delta}{\Delta x_i}\left[-u_i T + (\alpha_m + \alpha_s)\frac{\Delta T}{\Delta x_i}\right] \tag{7}$$

α_m and α_s are the molecular and subgrid components of thermal diffusivity, respectively. A modification of the interpolation of the nonlinear terms has been incorporated in the code as a result of thermal overshoot associated with the central-differencing algorithm originally used in our code. It is found that a first-order upwind interpolation can prevent cells having an extreme temperature gaining or losing further enthalpy, but the numerical diffusivity generated by this algorithm is larger than the subgrid-scale eddy diffusivity in our simulations. The standard second-order upwind interpolation is much less diffusive, but allows almost as much overshoot as the central difference scheme. By limiting the temperature at the mesh interface to its nearest physical extremum, a flux-limited second-order upwind scheme is constructed, which reduces the overshoot error to a minimum while retaining the accuracy of the interpolations.

No buoyancy effects are included, since these are of no interest in the present study, so the thermal and momentum fields are dynamically decoupled. The time step is kept well within the Courant and viscous limits, giving good temporal resolution of the fluctuating flow field. A full description of the simulation methods can be found in Gao et al. (1991) and Voke et al. (1995).

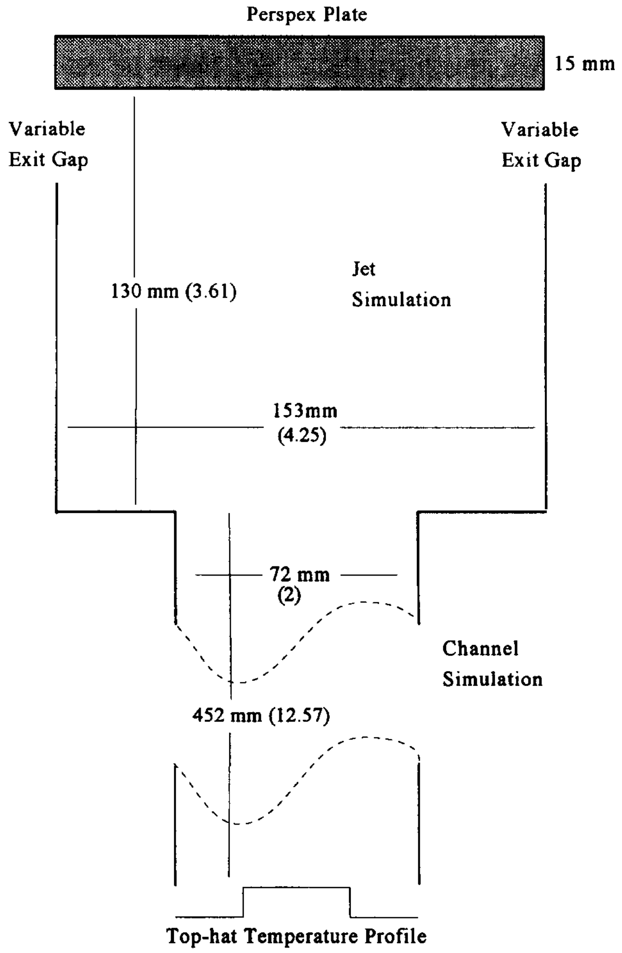

Figure 1 Geometry of the simulations, Cases 3 and 4; for Cases 1 and 2, the exit gaps are on either side of the plate, normal to the x direction; dimensions in mm for comparison with Morss (1991), and in units of the channel half-width h

Boundary conditions

The complete geometry, as shown in Figure 1, is planar. Dimensions are given both in terms of h, the half-width of the channel, equivalent to 36 mm in the jet experiments of Morss (1991), and in mm. In runs 3 and 4, the exit gaps are as shown, but in runs 1 and 2, they are normal to the x direction, on either side of the plate. The whole geometry is simulated in two separate runs, one for the channel upstream of the jet efflux plane (the channel simulation) and the other for the jet and also the impingement plate (the jet simulation). The two simulations are carefully matched: the velocity and temperature data on a plane perpendicular to the flow direction at the downstream end of the channel are recorded on disc at every time step in the channel simulation, and these data are subsequently read in to define the inflow velocity components and temperature for the jet simulation. The z direction, perpendicular to the plane of the diagram, is assumed infinite, and the velocity, pressure and thermal fields are assumed to be periodic in z. The absence of any upstream influence of the jet on the channel simulation is assumed to have negligible influence on the quantities of primary interest.

In the channel simulation, the velocity field is also periodic in the streamwise direction. The thermal boundary conditions are adjusted to produce a match to the experimental profiles at the jet efflux plane. At the upstream end of the channel, the temperature is forced to have a top-hat profile across the channel: the temperature field then develops naturally down the channel and is convected out at the end. The side walls of the channel and jet are adiabatic. On the impingement surface, the heat being conducted out of the fluid must be equal to the heat conducted into the solid. The temperature boundary condition on the rear surface of the plate is isothermal, with the temperature equal to the time-mean temperature of the fluid flowing out of the jet. Both the thermal and momentum boundary conditions of the jet outflow are advective,

$$\frac{\partial u_i}{\partial t} = -U_c \frac{\partial u_i}{\partial x_c} \tag{8}$$

$$\frac{\partial T}{\partial t} = -U_c \frac{\partial T}{\partial x_c} \tag{9}$$

The convective velocity U_c is the integrated mean normal velocity over the outflow plane, and x_c is the coordinate normal to the boundary. The outflow velocity at the new time step is updated using normalization algorithms reported by Voke and Potamitis (1994), which ensure exact mass balance between the inflow and outflow.

The solid wall boundary conditions are created according to the distance of the first mesh cell from the wall:

$$\begin{aligned} u_1^+ &= l^+ && \text{if} \quad l^+ \leqslant 5 \\ u_1^+ &= 5 + 5\ln(l^+/5) && \text{if} \quad 5 < l^+ \leqslant 30 \\ u_1^+ &= 5.455 + 2.5\ln(l^+) && \text{if} \quad 30 < l^+ \end{aligned} \tag{10}$$

The + superscript indicates viscous wall units,

$$l^+ = \frac{l u_\tau}{\nu_m}$$

$$u^+ = \frac{u}{u_\tau} \tag{11}$$

The value of friction velocity u_τ in the channel was used to provide a consistent normalization factor. The variable u_1^+ refers to the velocity of the first mesh cell away from the solid wall.

The computation of the wall stress varies, depending on the region wherein l^+ falls. This boundary condition is the same as the natural no-slip condition in the sublayer, but changes into one form of log-law model beyond $l^+ = 30$. In the channel simulation reported here, however, $l^+ = 6.01$, so the simulation has been run using the intermediate formula 10(b) which is the von Kàrmàn interpolation between the linear and logarithmic portions of the velocity profile. In the jet simulations, the natural (viscous) boundary conditions 10(a) apply to all the solid walls. This innovative approach appears to have worked very satisfactorily.

Subgrid-scale model

The subgrid-scale model used in the simulations is based on the original model of Smagorinsky (1963), in which a subgrid eddy-viscosity is derived from the local grid scale and strain rate:

$$\nu_s = (c_s \Delta)^2 (2 s_{ij} s_{ij})^{1/2} \tag{12}$$

in which the local grid scale is defined by

$$\Delta = (\Delta x \Delta y \Delta z)^{1/3} \tag{13}$$

The subgrid eddy-viscosity must reduce to zero when approaching the solid wall. This is achieved by modifying the length scale with a generalized van Driest (1956) near-wall damping function to cope with situations involving internal and external corners (Gao et al. 1991). The subgrid-scale constant is 0.1 in the channel simulation and 0.23 in the jet simulations. The resulting mean subgrid-scale eddy-viscosities are found to be low, less than three times the molecular viscosity.

A thermal subgrid-scale model is derived using a subgrid turbulent Prandtl number,

$$\alpha_s = \frac{\nu_s}{\mathrm{Pr}} \tag{14}$$

with the assumption that the subgrid-scale transport of enthalpy is closely related to that of momentum. A value of $\mathrm{Pr}_s = 0.3$ has been used in both the channel and jet simulations.

Results and discussion

Simulations performed

Four production jet simulations have been performed (Gao et al. 1991; Gao and Voke 1992) and a summary of the main flow and computational parameters is given in Table 1. Cases 1, 3, and 4 use a Prandtl number of 6.95, equal to that of water, and the plate has the conductivity of perspex. Case 2 differs from Case 1 in using a Prandtl number of 0.0213, chosen to reproduce the Peclet number 138.6 of an experiment by Morss (1991) with liquid sodium, and the conductivity of the plate is proportional to that of steel. Cases 1 and 2 are precisely the same in all boundary conditions, which has allowed the unambiguous identification of Prandtl number effects on the thermal dynamics, reported by Gao et al.

Prior to the production runs, the computer code was assessed in a number of tests, which included laminar jets, runs with half resolution, and runs to check the effects of subgrid-scale models, wall models, and flow boundary conditions. In the production runs, some time is allowed for the turbulent field to settle into a physically realistic state before time-averaged statistics are gathered. The production runs required over 80 CPU hours on a Cray X-MP or 50 h on a Y-MP.

The mesh resolution close to the plate is a limiting yet important factor in our simulations. The transfer of heat toward the plate by turbulent motions and into the plate by conduction are both likely to be affected by inadequate meshing in the plate

Table 1 Simulation runs, jet, and plate (dimensions in mm)

	Run 1	Run 2	Run 3	Run 4
Fluid	Water	Sodium	Water	Water
Plate	Perspex	Steel	Perspex	Perspex
Mean Re	6500	6500	6500	6500
Mean Pe	45,175	138.6	45,175	45,175
Exits normal to:	x	x	y	y
Exit gap	12.5	12.5	13.5	27
Δx (jet, min)	0.5	0.5	0.0028	0.0028
Δx (plate, min)	0.05	0.05	0.0014	0.0014
Δt	0.42 ms	0.42 ms	1.35 ms	1.35 ms
Total time	40.4 s	40.4 s	67.4 s	94.3 s

Table 2 Computational regions and meshes (dimensions in mm)

	Channel	Jet	Plate
N_x	64	63	9
N_y	32	68	56
N_z	64	64	64
L_x	452.4	130	15
L_y	72	153	126
L_z	113.1	113.1	113.1
Δx (max)	7.07	7.07	6.9
Δy	2.25	2.25	2.25
Δz	1.77	1.77	1.77

region. On the other hand, a very fine x mesh close to the plate results in a very tight Courant limit, since the fastest flow in the simulations is at the outflow regions on either sides of the plate. The computational mesh is, therefore, a compromise between the conflicting requirements of accuracy and economy. To resolve adequately the region close to the impingement plate, the x mesh is compressed slowly from the jet inlet to a significantly smaller spacing at the plate surface, then is stretched again inside the plate. A summary of the geometry and meshing is given in Table 2. The mesh in the z-direction is uniform. To increase the resolution near the impingement surface, the outflow gaps were changed to the side walls (normal to the y-direction) for Cases 3 and 4, as shown in Figure 1. The outflow gaps are 13.5 mm wide for Case 3 and 27 mm for Case 4. The Courant restriction is weaker so that we can run the simulations with finer resolutions near the impingement surface yet with bigger time steps (Table 2).

In Case 3, it is found that high acceleration of the flow through the narrow exit gaps induces a wall jet to develop along the impingement plate on either side of the center line. The wall jets have their own length and shear scales, and produce turbulence at position different from those where turbulence intensity peaks due to advection from the main impinging jet.

Analysis

Figure 2 shows profiles of the time-averaged stream-wise velocity and the root-mean-square (rms) fluctuation in the channel compared with the data of Nishino and Kasagi (1989). The comparison indicates that the channel simulation is quite satisfactory. The profiles of mean temperature and rms fluctuation at the jet efflux plane also compare well with the results from the impinging jet experiment (Morss 1991) in Figure 3, the deviations being accounted for by the difference between a planar and a circular geometry. (Mean and fluctuating temperatures are normalized by the maximum mean temperature in the plane,

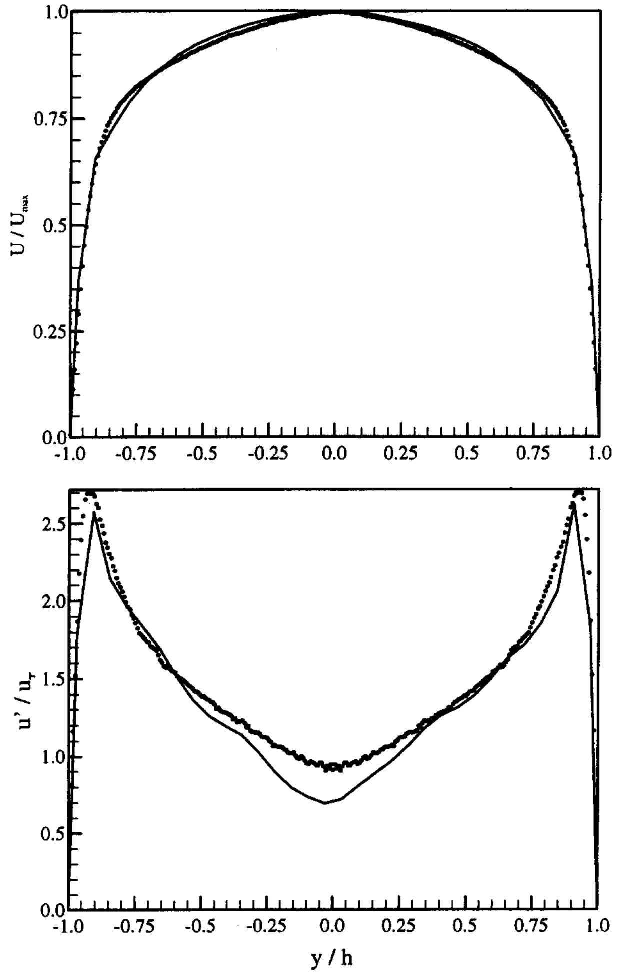

Figure 2 Profiles of (top) normalized mean streamwise velocity and (bottom) streamwise fluctuation u'/u_τ in the channel; line, simulation; symbols, Nishino and Kasagi (1989)

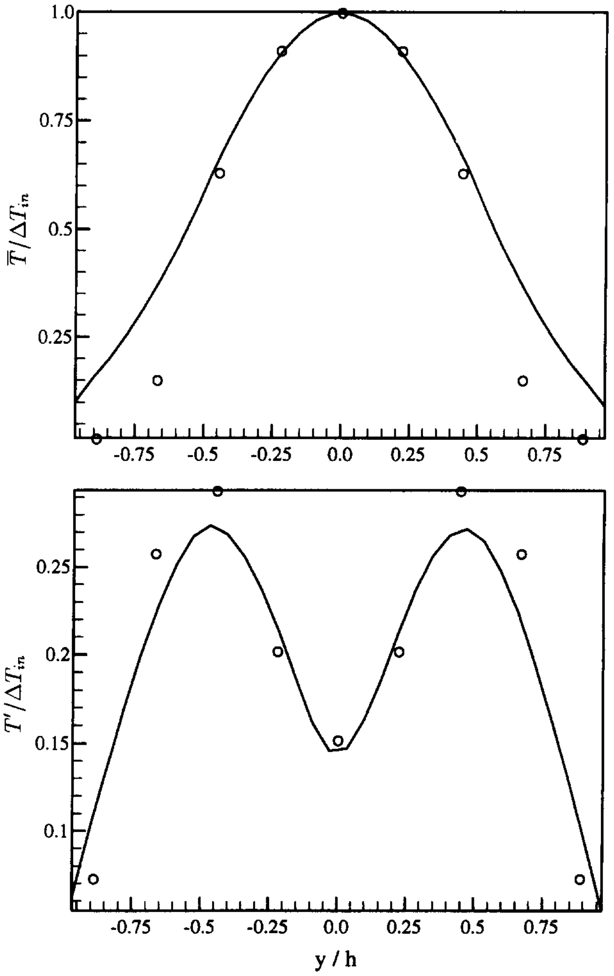

Figure 3 Profiles of (top) mean temperature and (bottom) temperature fluctuation T' at the jet efflux plane; line, simulation; symbols, Morss (1991)

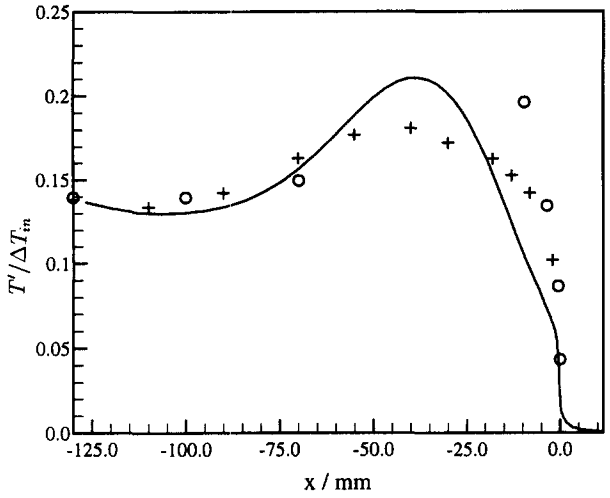

Figure 4 Streamwise profile of temperature (normalized by the maximum mean temperature difference at the jet efflux plane) at $y = 29$ mm; Line, simulation Case 4; circles, Morss (1991); crosses, closure computation of Ushijima (1991)

equal to 13.5°.) In the jet, the profile of the rms temperature fluctuation at $y = 29$ mm from Case 4 is compared with the results from the (cylindrical) experiment in Figure 4. The closure predictions of Ushijima (1991), also shown, confirm that the small deviation in this, as in other similar profiles, is primarily a geometric effect.

Figure 5 shows contours of the time-averaged stream-wise velocity in the jet simulation, very similar in shape to Morss (1991), confirming that the simulation reproduces the behavior of a physical jet. (x is negative since we measure from the impingement surface, $x = 0$.) The jet is decelerated as it approaches the impingment wall and greatly accelerated as it passes through the narrow exit gaps. The figure also clarifies the position of the twin recirculation regions. The bilateral symmetry of the simulation is reassuring, since the instantaneous fields are not at all symmetrical about the center line.

Figure 6 is produced by combining the mean temperature field in the jet with that in the channel through postsimulation processing, and shows clearly that in the channel, the temperature field develops gradually from the top-hat profile with sharp gradients (nominally 0 and 15° at the upstream end of the channel) into a smooth profile. In the jet, cool fluid is concentrated in the recirculation zones, while the center of the jet remains hot, and a layer of hot fluid spreads over the front surface of the plate. Further analysis reveals that this thin layer of hot fluid plays an important role in protecting the plate from the invasion of cold

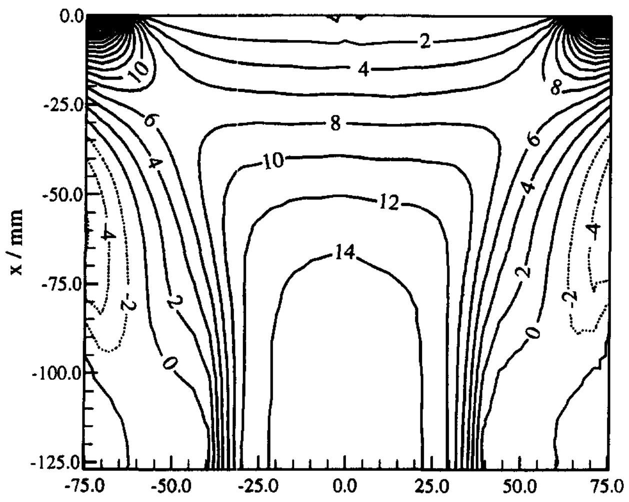

Figure 5 Contours of mean streamwise velocity u/u_τ in the jet; simulation, Case 1

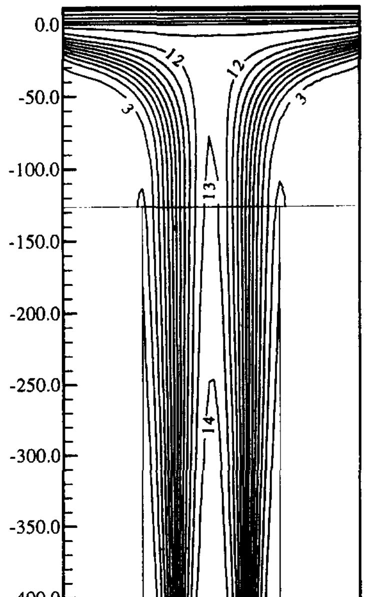

Figure 6 Contours of mean temperature in degrees in the channel and jet; (geometry not to scale); simulation, Case 4

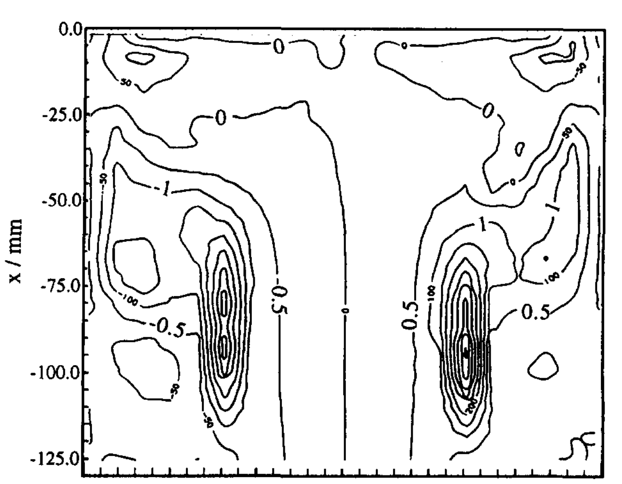

Figure 7 Contours of $\overline{u'v'}/u_\tau^2$ in the jet; simulation, Case 1

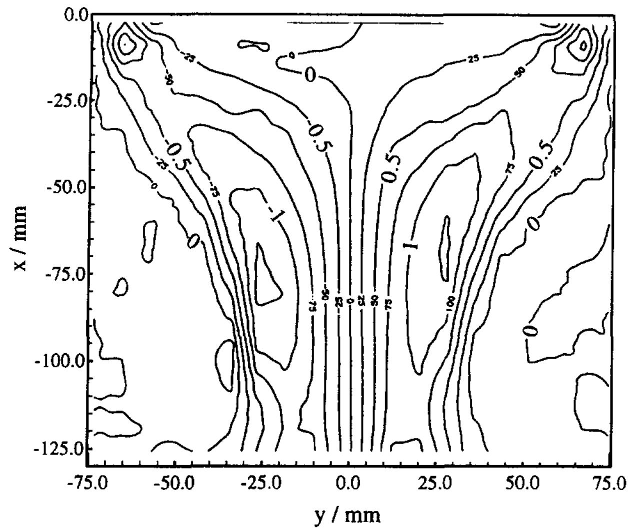

Figure 8 Contours of $\overline{v'T'}/u_\tau$/degree in the jet; simulation, Case 1

fluctuations. (Note that the aspect ratio of x- and y-axes is not physically proportioned in Figure 6.)

The striking localized peaks of the principal Reynolds stress $\overline{u'v'}$ and the lateral turbulent thermal flux $\overline{v'T'}$ in the jet, Figures 7 and 8, show that the turbulent fluctuations are amplified at the edges of the jet. Such an enhanced thermal transport across the jet edges can only come about from new hydrodynamic instabilities in the jet boundary, coupled with a strong temperature gradient. The presence of this temperature gradient is clear from the mean temperature distribution, as shown in Figure 6. In contrast, the stream-wise thermal flux $\overline{u'T'}$ (not shown) appears to be mainly a residue of the channel flow. The asymmetry in the time-averaged predictions arises from a lack of complete convergence in the statistics in regions such as the recirculation zones where fluctuations are large and of long period.

Instantaneous temperature data in an arbitrary transverse plane have been collected from our simulations, from which two video clips will be published for Cases 3 and 4 (Gao and Voke 1995). These show the dynamic process of the jets impinging on the solid plate. The video output also confirms that enhancement of pre-existing fluctuations in the channel upstream by new instabilities in the jet edges leads to entrainment of cool fluid from the recirculation zones. Identifiable cold eddies are thus formed in the jet edges, as shown in Figure 9(a). The eddies spread laterally and become thinner in the stream-wise dimension as they are convected onto the plate, Figure 9(b). The effect is also present in the sodium simulation, but is less obvious because of the diffusing effect of the higher conductivity. The video sequences also indicate that there occasionally exist strong eddy movements in the span-wise direction in the impingement area; further study is needed to account for this quantitatively.

We particularly emphasize here that it is from these and other similar instantaneous thermal fields that the smooth temperature distribution shown in Figure 6 is obtained through span-wise and time averaging, and that other important quantities discussed below, vital to reactor safety design and analysis, are derived. One can hardly imagine from information like Figure 6 the real pictures of thermal fluctuation typified by Figure 9. This is one of the limitations that closure modeling suffers: it can only produce averaged quantities similar to Figure 6.

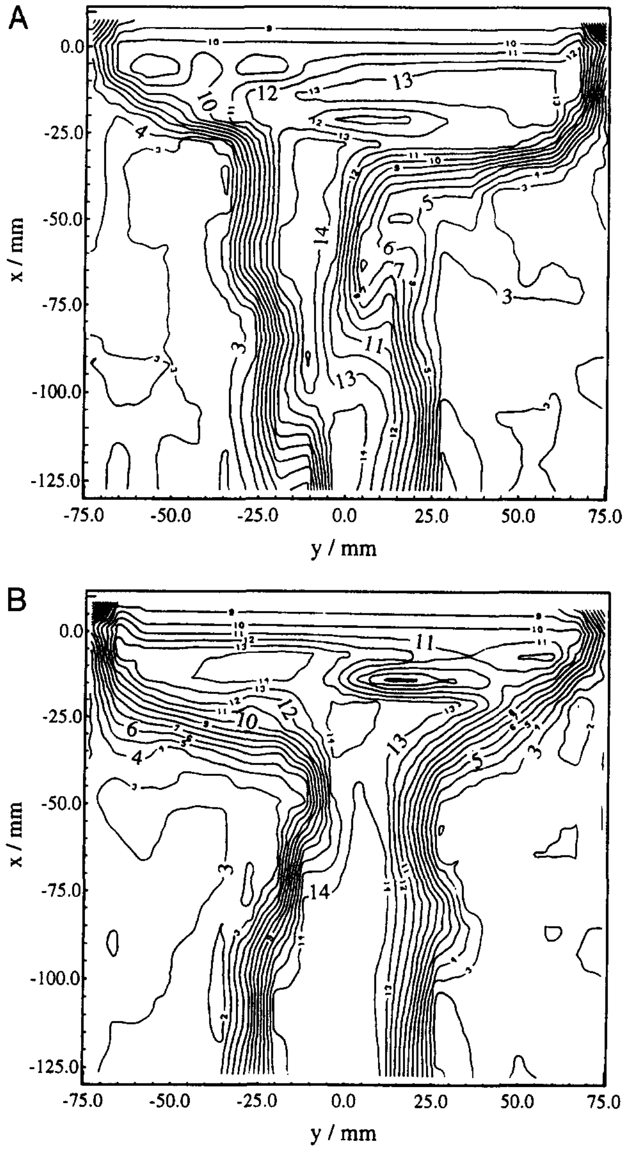

Figure 9 Instantaneous temperature field in degrees on a single z plane; (a) at time $t = 29.0$ s; (b) at time $t = 30.3$ s; simulation, Case 4

High lateral two-point correlations of temperature are measured in the experiments of Morss (1991) and confirmed by the simulations, Figure 10. The correlations shown are

$$R_{TT}(\delta t,\ x,\ y,\ y+\delta y) = \frac{\Sigma_{t_0}^{t_N} T'(t,\ x,\ y) T'(t+\delta t,\ x,\ y+\delta t)}{\left[\Sigma_{t_0}^{t_N} T'(t,\ x,\ y) \Sigma_{t_0}^{t_N} T'(t+\delta t,\ x,\ y+\delta y)\right]^{1/2}} \qquad (15)$$

where $t_N - t_0 = N\Delta t$. (Note the distinction between the time displacement variable in the correlation δt and the simulation time step Δt.) From the detailed simulations of the distortion of thermal eddies in the impingement region it is concluded that the lateral spreading of eddies is the main dynamical cause. The correlations between temperatures in the fluid and in the solid plate are also of particular importance. These are all very high at zero time separation. The high correlations suggest that the temperature inside the solid is determined almost entirely by the fluid temperature on the impingment surface at the same lateral position. To test this, a simple one-dimensional (1-D) conduction model was constructed, taking the temperature history at the point just outside the plate from the simulation as a forcing input.

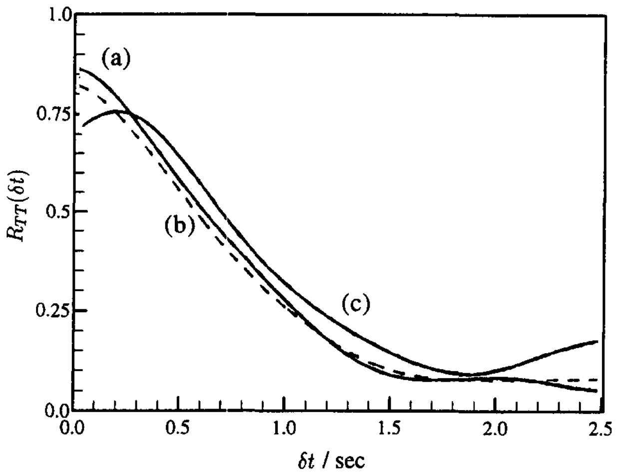

Figure 10 Normalized temporal cross-correlations of temperature in the fluid, $R_{TT}(\delta t, x, y, y+\delta y)$ for $(x, y) = (-0.5, 0)$ mm and (a) $\delta y = 29$ mm; (b) $\delta y = 43$ mm; (c) $\delta y = 58$ mm; simulation, Case 1

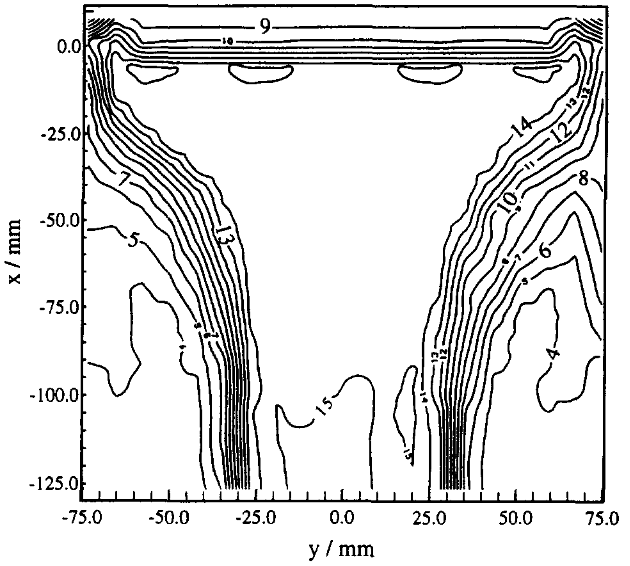

Figure 12 Contours of maximum temperature in the jet, in degrees; Case 1

The results, although giving a slightly higher temperature variation on the solid surface, are almost indistinguishable from the corresponding 3-D simulation, suggesting that it is sufficient to be able to predict the thermal dynamics of the turbulence in the jet: the prediction of transmission of thermal fluctuations into the plate is straightforward. Further details of the thermal interaction between the fluid and solid plate will be published elsewhere (Voke and Gao 1995).

The maximal temperature difference (peak-to-peak swing) is a key quantity in reactor safety analysis, but is beyond the reach of closure models. Such information has also been derived from the present simulations, and Figure 11 shows the distribution for Case 1. The shape of the distribution is very similar to that of the rms temperature fluctuation (not shown) for both water and sodium runs. The origin of this trend is clarified by studying the distributions of the maximal and minimal temperatures, Figures 12 and 13, occuring during the sampling period of Case 1. The maximum temperatures are consistently high in the jet center right up to and into the plate. The minimum values, on the other hand, show a much greater variation as the plate is approached. It appears that the plate surface is protected by a layer of hot fluid (higher than 8°), and incursions of cold fluid into this layer close to the plate are truly rare. Study of probability distributions of these extreme events has confirmed this. The ratio of peak-to-peak swing and rms fluctuation, known as crest factor, has also been studied.

The temperature swings experienced in the impingement region are much lower than those between the hot central core of the jet and the recirculation zones, because the cold eddies are diffused while they move toward the plate. This suggests that design methods based on the maximum temperature swing at the jet efflux plane, although acceptably safe, produce a rather conservative design. For liquid sodium, the diffusion is very much greater, and the peak-to-peak fluctuations downstream are correspondingly lower.

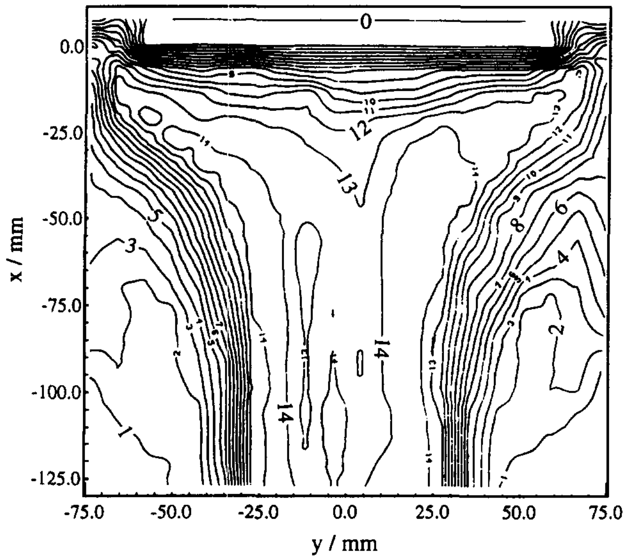

Figure 11 Contours of peak-to-peak temperature swing in the jet, in degrees; simulation, Case 1

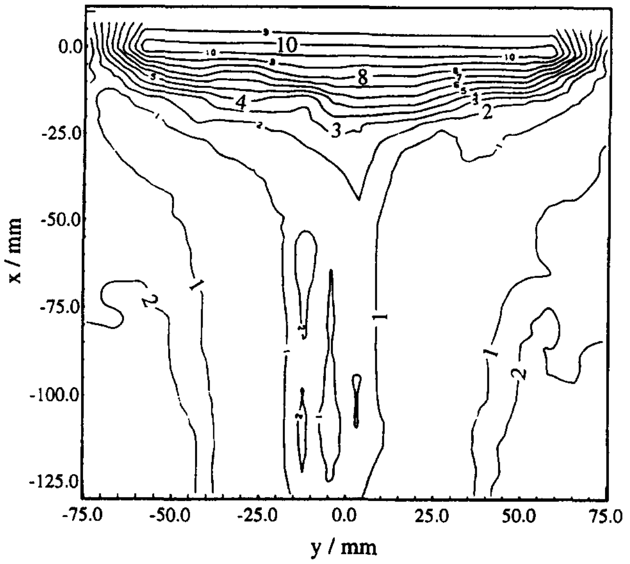

Figure 13 Contours of minimum temperature in the jet, in degrees; Case 1

Conclusions

The preceding results show that the LES predictions of mean quantities and low-order statistics are in sufficient agreement with the experiments and closure calculations to give confidence in the fidelity of the LES. Quantities such as peak-to-peak swing, derived from the simulations, can provide reactor designers with important information for estimating the magnitude of thermal striping effects.

The instantaneous thermal fields have been studied in some detail for certain of the cases simulated, revealing the mechanisms governing the generation and transportation of thermal eddies from the jet into the solid structure. It is found that for a jet with a hot core and cool edges, cool fluid accumulates in the recirculation zones, while hot fluid is spread over the plate as the jet impinges. The instantaneous thermal distributions and video output have proved that the thermal fluctuations originating from the channel are further enhanced by instabilities at the jet edges which entrain cool fluid from the recirculation zones into the jet. The eddies become elongated laterally as they move toward the impingement plate, resulting in high lateral two-point temperature correlations.

We have also proved that the temperature fluctuations inside the plate depend almost entirely on the fluctuations at the impingement surface at the corresponding *y* position, leading to a simple 1-D model for the solid-phase heat transport. The thermal correlation length is much lower in the direction perpendicular to plate for the water, while for the sodium, the structures are larger and the correlation length is significantly increased.

Acknowledgments

This research was performed under grants GR/F 26089, GR/H 16315, and CON/BC/2264 supported by the Central Electricity Generating Board (later Nuclear Electric plc) and the U.K. Science and Engineering Research Council. We gratefully acknowledge the support from the technical correspondents at Berkeley Nuclear Laboratory, Richard Szczepura and Tony Morss.

References

Gao, S., Leslie, D. C. and Voke, P. R. 1991. Large-eddy simulation of thermal impinging jets. Rep. ME-FD/91.02, Dept. of Mechanical Engineering, University of Surrey, Guildford, GU2 5XH, UK

Gao, S. and Voke, P. R. 1992. Further large-eddy simulation of a thermal impinging Jet. Rep. ME-FD/92.05, Dept. of Mechanical Engineering, University of Surrey, Guildford, GU2 5XH UK

Gao, S. and Voke, P. R. 1995. The evolution of thermal eddies in a numerically simulated turbulent jet. *Vis. Eng. Res.*, to be published

Morss, A. 1991. Impinging jet results at low Reynolds numbers for comparison with large-eddy simulation calculations. Nuclear Electric Memorandum TD/STB/MEM/0276, Technology Division, Nuclear Electric, Berkeley, Glos., UK

Nishino, K. and Kasagi, N. 1989. Turbulence statistics measurements in a two-dimensional channel flow using a three-dimensional particle tracking velocimeter. *Proc. 7th Symposium on Turbulent Shear Flows*, Stanford University, Stanford, CA

Schumann, U. 1975. Subgrid scale model for finite difference simulations of turbulent flows in plane channels and annuli. *J. Comp. Phys.*, **18**, 376–401

Schwarztrauber, P. N. 1974. A direct method for the discrete solution of separable elliptic equations. *SIAM J. Num. Analysis*, **11**, 1136–1150

Smagorinsky, J. 1963. General circulation experiments with the primitive equations: Part I, the basic experiment. *Monthly Weather Rev.*, **91**, 99–164

Ushijima, S. 1991. FEAT calculations on impinging jets with different geometries and inlet conditions. Nuclear Electric Memorandum TD/NS/MEM/0495, Technology Division, Nuclear Electric, Berkeley, Glos., UK

van Driest, E. R. 1956. On turbulent flow near a wall. *J. Aero. Sciences*, **23**, 1007

Voke, P. R., Gao, S. and Leslie, D. 1995. Large-eddy simulations of plane impinging jets. *Int. J. Num. Methods Eng.*, **38**, 489–507

Voke, P. R. and Gao, S. 1995. Numerical study of heat transfer from an impinging jet, in preparation

Voke, P. R. and Potamitis, S. G. 1994. Numerical simulation of a low-Reynolds-number turbulent wake behind a flat plate. *Int. J. Num. Methods Fluids*, **19**, 377–393